Available online at www.sciencedirect.com

Cement and Concrete Research 37 (2007) 894 – 901

Moisture transport in heated concrete, as studied by NMR, and its consequences for fire spalling

G.H.A. van der Heijden, R.M.W. van Bijnen, L. Pel *, H.P. Huinink

Transport in Permeable Media, Eindhoven University of Technology, Department of Applied physics, 5600 MB Eindhoven, The Netherlands

Received 31 October 2006; accepted 5 March 2007

Abstract

During the past 30 years concrete has developed enormously in both strength and durability. A drawback of these improvements is the increased risk of explosive spalling in case of fire. The moisture inside the concrete plays an important role in the spalling mechanism. In order to study the moisture migration inside concrete during intense heating, a dedicated nuclear magnetic resonance (NMR) setup was built. This setup can be placed inside a 1.5-T MRI scanner.

With this setup one-dimensional moisture profiles can be measured while the concrete sample is heated up to 250 °C. Besides concrete, measurements were performed on fired-clay brick and calcium-silicate brick.

The results show that water inside the concrete sample is superheated to a temperature of 170 °C, which results in an increased pressure inside the concrete. A model was developed to predict the movement of the observed drying front.

Keywords: Nuclear magnetic resonance; Fire spalling; Concrete (E); Permeability (C); Transport properties (C); Modeling (E); Temperature (A)

1. Introduction

Over the past decades concrete has improved in both strength, workability and durability, and the research on concrete still continues [1]. Ordinary concrete (OC) has evolved in so-called high performance concrete (HPC), which is commonly used in modern structures like tunnels, bridges and buildings. In order to achieve a higher strength and better durability the water cement ratio is reduced. As a result, the porosity and more important, the permeability of the concrete are also greatly reduced. Due to these modifications an increased danger of (violent) spalling is present when the concrete is subjected to high temperatures as occur in a fire [2–5].

Two mechanisms are assumed to be responsible for spalling. First, upon heating the moisture inside the concrete will evaporate and depending on the pressure will boil at a certain temperature. The escaping water vapor is hindered by the very low permeability, and as a result the pressure inside the pores increases. If the pore pressure exceeds the tensile strength of the concrete, it can result in different forms of spalling. Second, due to the difference in thermal strain between the cement and the aggregates, thermal stresses occur in the material. The temperature gradient resulting from one-sided heating generates compressive stresses on the surface, which results in internal cracking. In most cases a combination of both mechanisms described above is needed for spalling to occur [4]. A number of additional factors, e.g., phase changes of crystals, section shapes, applied loading and aggregate size, can be detrimental to the structural integrity and spalling resistance of concrete. However, the role of moisture and vapor in fire spalling is still relatively unknown; therefore, our focus in this paper will be on moisture and vapor transport and its influence on fire spalling of concrete.

In addition to full scale experiments, numerous mathematical models have been used to predict moisture transport and the spalling behavior of concrete [6–8]. In these models

---

* Corresponding author. Tel.: +31 402473406; fax: +31 402432598.
E-mail address: l.pel@tue.nl (L. Pel).

0008-8846/$ - see front matter © 2007 Elsevier Ltd. All rights reserved.
doi:10.1016/j.cemconres.2007.03.004

measurements of temperature and pressure are generally used for validation. No direct measurements of the moisture content are available. With NMR it is possible to non-destructively measure the moisture content inside porous building materials [9,10]. In this paper we describe a study in which NMR is used to measure the moisture content inside a porous material, e.g., concrete, during intensive heating. We have constructed a model based on vapor fluxes and a receding drying front that explains the high pore pressures in concrete.

2. Theory

In this section a model will be introduced that describes the movement of the drying front based on the vapor flux that results from evaporating water at this drying front. The influence of different parameters, such as permeability, porosity and temperature on the movement of the drying front will be discussed. The aim of our model is to determine the amount of influence that moisture and vapor alone have on fire spalling of concrete.

2.1. Model

Consider a semi-infinite half-space filled with a wet porous material, which is uniformly heated at its surface (see Fig. 1). The geometry of the system allows us to use a 1D description, with the distance to the heated surface x as the only spatial variable. The heating causes the temperature to rise everywhere in the material. As a consequence water will evaporate and a drying front will develop in the material at which the liquid pore water boils to vapor. If this drying front is a sharp front, we can divide the material in a dry part, and a wet part with a saturation S, which denotes the pore volume occupied by liquid water relative to the total pore volume.

To construct an equation for the position u of the drying front, we introduce some additional simplifications. First, the temperature in the material T [°C] is assumed to be independent of the position of the drying front, i.e., $T=T(x, t)$, with x the depth into the material and t the time. This assumption applies that the latent heat of liquid water can be neglected compared to the heating of the solid matrix, which may be correct for materials with a low porosity, such as concrete, since the relative water content is low. For such a situation the temperature $T=T(x,t)$ is theoretically given by [11]

$$T(x,t)=T_0+\frac{2F_0}{K}\left(\sqrt{\frac{\kappa t}{\pi}}\exp\left(\frac{-x^2}{4\kappa t}\right)-\frac{x}{2}erf\left(\frac{x}{2\sqrt{\kappa t}}\right)\right), \quad (1)$$

with F_0 [W m^{-2}] the heat flux, T_0 the temperature at $t=0$, K [W m^{-1}°C^{-1}] the thermal conductivity of the material and κ [m^2 s^{-1}] the thermal diffusivity. At $t=0$ and $x>0$ the temperature is T_0, and for $x=0$ (the heated surface) a constant heat flux (F_0) is applied for $t>0$. We will also neglect dehydration as a moisture source and heat sink. The total amount of water that can be released by dehydration is significant, but the rate of this dehydration process is very slow compared to the vaporization process. Second, we will assume that the liquid water content of the wet part is constant. This assumption implies that the moisture transport in the wet part of the material can be neglected, which we believe to be a reasonable assumption. We expect the pressure in the material to be highest at the drying front since in the wet part the temperature decreases when moving away from the drying front, and in the dry part the water vapor can escape through the pore network and the external surface. Close to the surface the pressure must be equal to the outside (atmospheric) pressure, hence the pressure must continuously decrease from the drying front to the material surface [2,4,12,13].

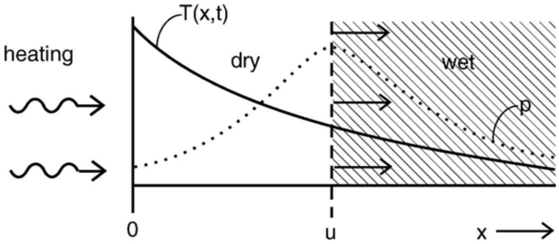

Fig. 1. Schematic overview of the model. The porous material is heated uniformly at its surface ($x=0$). Due to the heating the temperature $T(x,t)$ rises (solid line), and a receding drying front moves into the sample. This front is located at $x=u(t)$ and separates the material into a dry and a wet part. The pressure (dotted line) will be highest at the drying front.

Driven by the boiling process, the drying front will recede into the material, and its speed will be governed by the vapor flux from the drying front to the external surface. When the drying front advances a distance du in a time dt, a liquid water quantity per unit area of nS_0du is converted to vapor, where n is the porosity. This generates a vapor mass-flux J_v from the drying front to the external surface

$$J_v=-\frac{nS_0}{V_m}\frac{\partial u}{\partial t}, \quad (2)$$

with V_m the molar volume of liquid water. The vapor transport is assumed to be a viscous flow driven by the pressure gradient. The vapor is transported mainly through the larger pores. In this range of pore sizes, temperatures and pressures the vapor is in the continuum regime (i.e., the mean free path of a molecule is much smaller than the typical pore size [14]). Moreover, vapor is assumed to be the only gas phase present, and the influence of other gases such as CO_2 generated at high temperatures is neglected. Therefore, the vapor flux can be calculated from Darcy's law. We assume that the temperature gradient does not influence the vapor flux in the dry part, and that the vapor behaves as an ideal gas. The vapor flux J_v can now be expressed as a volume flux q times the density:

$$J_v=q\rho=-\frac{k}{\mu}\frac{\partial p}{\partial x}\frac{P}{RT}, \quad (3)$$

where k [m^2] is the intrinsic permeability, μ [kg m^{-1}s^{-1}] is the kinematic viscosity of vapor, p is the pressure and R is the ideal gas constant. Note that we have used the fact that $p=\rho RT$. The pressure at the drying front depends on the temperature at which the water boils and is given by the empirical Antoine equation:

$$ {}^{10}\log\left(\frac{P}{D}\right) = A - \frac{B}{T+C} \tag{4}$$

with the constants $A = 8.07$, $B = 1731$, $C = 233$ and $D = 133$ [15]. By substituting Eq. (3) in Eq. (2) and assuming a quasi-stationary situation, the following differential equation for the position of the drying front is found:

$$\frac{\partial u}{\partial t} = \frac{kV_m}{2\mu RTnS}\frac{\Delta p^2}{u} \tag{5}$$

Eqs. (1), (4) and (5) form a closed set of equations, which can be solved numerically to investigate the influence of different parameters on the movement of the drying front.

Although we have made several simplifying assumptions, our model already contains a mechanism that could account for the explosive spalling of concrete. Moreover, the model can be extended to account for more influences, which will merely complicate numerics. For instance, moisture transport within the wet part of the material will add a coupled differential equation for S, but leave Eq. (5) intact. Dehydration reactions in concrete can be added as a temperature dependent source term. Similarly, vapor transport within the wet part and/or taking the temperature gradient in the dry part into account are conceptually easy to implement by adjusting the expressions for vapor fluxes, but maintaining the central idea of a balance between them.

2.2. Model predictions

In Eq. (5) several important parameters can be identified, which influence the speed of the drying front. Most important is the permeability, which can vary over several orders of magnitude, depending on the material. The speed of the drying front is proportional to the permeability. The pressure at the drying front has a similar influence; large pressures yield a fast moving drying front. In materials with a high porosity and water content the drying front moves slower, because a larger amount of water has to evaporate. When the drying front is receding further into the material, the speed will decrease due to the increasing distance that the vapor has to move before leaving the material.

In Fig. 2 the predictions from the model are illustrated for two different materials, fired-clay brick, with a permeability of 10^{-14} m^2 and a porosity of 20 %, and concrete, with a permeability of 10^{-18} m^2 and a porosity of 7 %. In Fig. 2a the drying front positions for brick and concrete are shown as a function of time. The 100 °C isotherm is included as a reference, indicating the position at which the water would boil at a pressure of 1 bar. It is clear that the drying front in brick can follow the 100 °C isotherm more easily than in concrete. As a consequence the temperature, and hence the pressure, at the

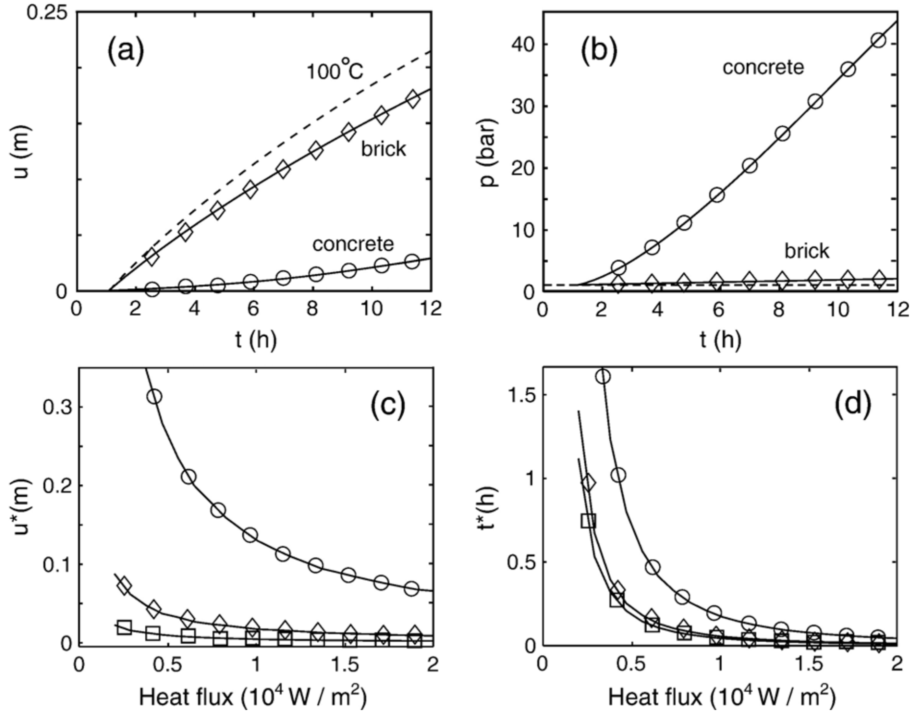

Fig. 2. (a) Position u of drying front as a function of time according to Eq. (5), for concrete (permeability $k=10^{-18}$ m^{-2}, porosity $n=0.1$, ○) and fired-clay brick ($k=10^{-14}$ m^{-2}, $n=0.2$, ◇), heated at the surface with a constant flux of 5000 W m^{-2}. The dashed curve marks the position of the 100 °C isotherm. The front starts to move after about 1 h, as the material heats up to 100 °C first. (b) Calculated pressure at the drying front, for concrete (○) and brick (◇). The dashed line marks atmospheric pressure (1 bar). (c) Depth at which a critical pressure of 50 bar is exceeded, as a function of the heat flux into the material, for various permeabilities: $k=10^{-17}$ m^{-2} (○), $k=10^{-18}$ m^{-2} (◇) and $k=10^{-19}$ m^{-2} (□). (d) Time at which the critical pressure of 50 bar is exceeded, as a function of the heat flux into the material, for the permeabilities as in panel c.

drying front is higher in concrete than in brick (see Fig. 2b). The pressure at the drying front reaches 40 bar in concrete, whereas in brick it remains close to 1 bar.

In order to make some predictions regarding spalling behavior, a reference pressure of 50 bar (5 MPa) is chosen. This pressure is chosen because it reflects the typical tensile strength of an HPC. When this pressure is exceeded, possible cracking and explosive spalling can occur [13]. Fig. 2c shows the depth u^* at which this critical pressure is exceeded first, as a function of the heat flux into the material and for several permeabilities that are typical for concrete. For high heat fluxes the spalling would occur close to the surface, whereas lower heat fluxes would result in spalling deeper into the material. Similarly, Fig. 2d shows the time t^* at which this critical pressure is exceeded as a function of the heat flux into the material. High heat fluxes cause quick spalling, and lower heat fluxes delay spalling. Again the same typical values for the permeability are used. This predicted behavior is in good agreement with empirical observations [16], where a rapid increase in temperature is known to cause a fast spalling of small pieces of material, and a slow temperature increase causes a delayed spalling, which is more violent and involves larger chunks of material.

3. NMR

3.1. NMR principle

Almost all nuclei have a magnetic dipole moment, resulting from their spin momentum. When a nucleus with a net nuclear magnetic moment is placed in an external magnetic field B_0, the moment precesses at a certain resonance frequency. This resonance frequency is also called the Larmor frequency f_l [Hz] and depends on the magnetic field:

$$f_l = \frac{\gamma}{2\pi} B_0, \tag{6}$$

where γ is the gyromagnetic ratio. This ratio depends on the nucleus, and therefore it is possible to measure different types of nuclei by changing the resonance frequency. In our measurements only hydrogen is measured in order to obtain the moisture distribution (for ^{1}H $\gamma/2\pi = 42.58$ MHz T^{-1}). At 1.5 T the resonance frequency equals 63.9 MHz.

The individual moments all contribute to a net nuclear magnetization. In equilibrium the net magnetization is aligned parallel to B_0. The direction of the net magnetization can be manipulated by applying a radiofrequent magnetic field B_1 at the resonance frequency. In our experiments the magnetization induces a signal in the measurement coil, which is the so-called 'Hahn-spin echo' [17]. The signal intensity S is given by [18]:

$$S = k\rho\left[1 - \exp\left(-\frac{\mathrm{TR}}{T_1}\right)\right]\exp\left(-\frac{\mathrm{TE}}{T_2}\right), \tag{7}$$

In this equation k is a proportionality constant, and ρ is the density of nuclei. The signal S does not only represent the density of nuclei, it also gives information about the rate at which the net magnetization relaxes to its equilibrium. The relaxation due to the interaction of spins with the surroundings is called the spin-lattice relaxation and is represented by T_1. The relaxation due to spin–spin interactions is represented by T_2. Especially the spin–spin relaxation can give information about the distribution of pore sizes in a porous material [10,19].

In Eq. (7) the repetition time TR and the echo time TE are the two important experimental parameters. The spin echo signal S is recorded after a time TE which is usually in the order of 200–600 μs. The relaxation time T_2 of water in a porous building material can be as short as 500 μs. The spin echo needs to be recorded before the signal has decayed. The repetition time is the time in between two successive spin echoes. To improve the signal-to-noise ratio a typical NMR measurement is repeated a number of times for averaging. Typically TR > 4T_1 is chosen. Water in a porous material has a relaxation time T_1 in the order of 0.1–0.5 s.

In a homogeneous magnetic field B_0 all ^{1}H nuclei have the same resonance frequency, and as a result a signal from the whole sample is obtained. By making the magnetic field position dependent one can selectively excite the nuclei in a limited volume of the sample, making it possible to measure spatial distributions of water. In our case the modified magnetic field is given by:

$$B(x) = B_0 + Gx, \tag{8}$$

where x is the position in the sample along the direction of the gradient G [T m^{-1}] (see Fig. 3). By varying the frequency the signal can be measured at different positions in the sample without moving the sample.

3.2. NMR setup

The experiments were performed with a home-built NMR setup which was especially designed for moisture measurements on building materials. A schematic diagram of the setup is shown in Fig. 3. The main magnetic field is provided by a 1.5-T medical scanner (Gyroscan, Philips). The setup can be

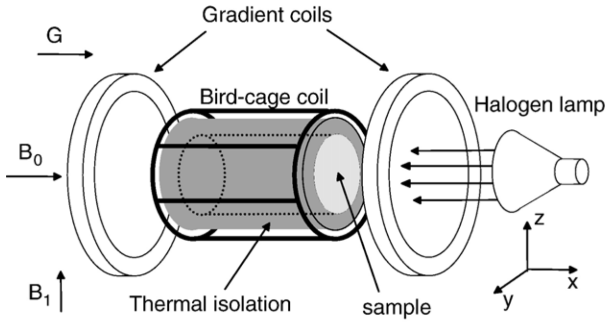

Fig. 3. Schematic diagram of the NMR setup. A 1.5-T MRI scanner provides the main magnetic field B_0. Two Helmholtz coils provide a gradient G of 86.5 mT m^{-1} in the x direction. A birdcage coil is used for both applying RF pulses B_1 and receiving the NMR signal. A halogen lamp is used to heat the sample, which is thermally insulated and positioned within the birdcage coil.

placed in the bore of the magnet. Two Helmholtz coils provide the magnetic field gradient G in the direction of B_0. The magnitude of the gradient is 86.5 mT m^{-1}, providing a spatial resolution of 1 mm. A home-built birdcage coil is used for applying the RF pulses (B_1) and receiving the NMR signal from the sample. The coil is 60 mm long and has a diameter of 60 mm.

A birdcage coil is used because it generates a homogeneous B_1-field perpendicular to the sample. Therefore, the coil can be placed parallel to the main magnetic field providing optimal use of the available space inside the bore. The sample is heated with a halogen lamp. The reflector of the lamp was gold plated to ensure maximum reflection of the infra-red radiation. The sample is placed inside the birdcage coil and is thermally insulated using mineral wool. This thermal insulation also limits the heating of the coil.

4. Materials and methods

Three different samples have been investigated: fired-clay brick, calcium-silicate brick and a B40 concrete. The samples all have a diameter of 40 mm. The calcium-silicate and concrete samples are 40 mm long, and the fired-clay brick sample is 60 mm long. In Table 1 the mean pore size, permeability [20] and porosity of the three samples are given. Mean pore size and porosity were measured by mercury intrusion porometry (MIP). The permeability of the fired-clay brick was measured using a constant head permeameter. The concrete sample has the lowest porosity, pore size, and permeability followed by the calcium-silicate brick and then fired-clay brick.

The samples are capillary saturated after which they are tightly fitted in a PTFE sample holder. Teflon is used because it does not contain hydrogen. The liquid water or vapor can only escape from the heated surface. In this way a one-dimensional experiment is created and a pressure build up inside the sample is possible.

The fired-clay brick sample was heated with 50 W and the calcium-silicate brick and concrete samples with 95 W. The measuring time of one profile depends on the number of averages needed. However, to ensure a good temporal resolution the measurement time was limited to 10 min. Thermocouples (type K) were placed at eight positions in the fired-clay brick and calcium-silicate brick sample and at five positions in the concrete sample. The thermocouples were positioned in drilled holes with a diameter of 2 mm and were sealed using PTFE tape. First a moisture and temperature profile is measured. Next, the heating is turned on. The first moisture profile of the saturated sample is used as a reference to correct for the coil profile.

Table 1
Mean pore size, permeability and porosity of the three samples: concrete, calcium-silicate brick and fired-clay brick

	Fired-clay brick	Calcium-silicate brick	Concrete
Permeability [m^2]	10^{-12}*	10^{-13}–10^{-16}	10^{-17}–10^{-18}
Porosity [m^3 m^{-3}]	0.25*	0.20*	0.07*
Mean pore size [nm]	4100*	890	15*

The measured values are indicated with an *. Mean pore size and porosity were measured by mercury intrusion porometry (MIP). The permeability of the fired-clay brick was measured using a constant head permeameter. The other values are from [20].

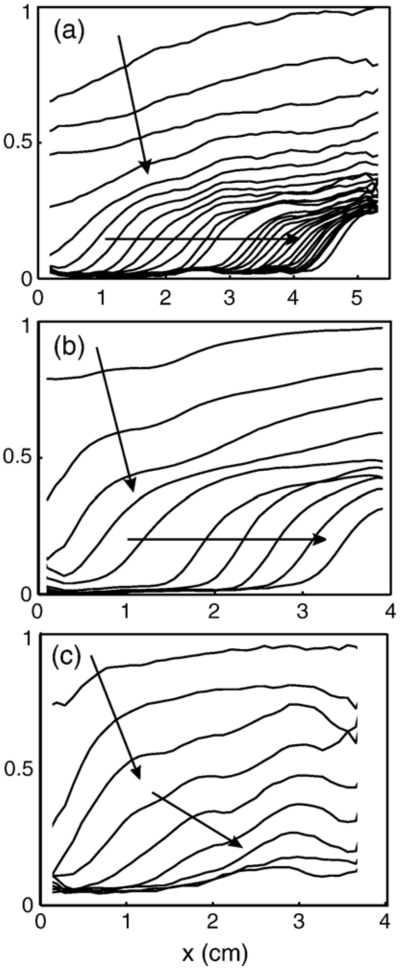

Fig. 4. Experimental moisture profiles for (a) fired-clay brick, (b) calcium-silicate brick and (c) concrete. The vertical axis corresponds to the saturation S, and the horizontal axis is the position in the sample ($x=0$ corresponding to the heated surface). Initially the sample is fully saturated ($S=1$). The time between two subsequent profiles is 10 min.

5. Results

In this section the results from the NMR measurements on fired-clay brick, calcium-silicate brick and concrete will be presented. First, the measured moisture profiles will be presented in Section 5.1. The profiles were measured using the NMR setup described in the previous section. Next, the results from the temperature measurements will be discussed in Section 5.2. Finally, the predictions from the model presented in Section 2 will be compared with the measurements.

5.1. Moisture profiles

The measured moisture profiles are shown in Fig. 4. The moisture profiles are shown for (a) the fired-clay brick, (b) the calcium-silicate brick and (c) the concrete sample. The vertical axes represents the saturation, with $S=1$ corresponding to a fully saturated sample. The horizontal axes represents the position x in the sample with $x=0$ corresponds to the position of the heated surface. The time between two subsequent profiles is 10 min.

In fired-clay brick the moisture remains homogeneously distributed during the initial drying period (first 40 min). In this stage the pore system is still percolated with liquid water, and moisture can be transported by liquid flow to the heated surface where it evaporates. However, when a certain critical moisture content is reached a receding drying front develops, indicating that the drying is limited internally by the transport of vapor to the external surface. The same behavior can be observed in calcium-silicate brick, however, in concrete this drying front is less pronounced.

5.2. Temperature profiles

The temperature was also measured during the experiments at different positions in the samples. In Fig. 5 the temperature profiles for (a) fired-clay brick, (b) calcium-silicate brick and (c) concrete are shown every 10 min. The vertical axis represents the temperature and the horizontal axis the position in the sample measured from the external surface. The positions of the thermocouples are indicated on the first temperature profile (●). The positions of the drying front with the corresponding temperature at the drying front are also shown (▼). The position of the drying front is associated with maximum slope in the moisture distribution.

The main difference between the three materials is the influence of evaporating and boiling water on the temperature increase. Evaporating water has a cooling effect. Therefore, the initial temperature increase for the two types of brick stalls at 70–80 °C. The temperature further increases after the initial uniform drying period ends, and a drying front develops. Furthermore, in both the fired-clay brick and the calcium-silicate brick the temperature increase stalls at 100 °C due to the presence of boiling water, whereas in concrete the influence of boiling water is less pronounced. The reason is the large porosity and hence water content of the bricks, 22% and 25 %, respectively, compared to concrete (7%).

The temperature at the drying front increases above 100 °C for concrete, with a maximum temperature of 170 °C (see Fig. 5). In the calcium-silicate brick the temperature remains at 115 °C, whereas in fired-clay brick the temperature decreases from a maximum value of 110 °C to 100 °C. It is assumed that the highest pore pressures are reached at the drying front, therefore the temperature on the drying front was used to estimate the pressure using Eq. (4). For fired-clay brick the maximum temperature of 110 °C corresponds to a pressure of 1.5 bar. For calcium-silicate brick (115 °C) a maximum pressure of 2 bar, and for concrete 10 bar (170 °C). It must be noted that these pressures are only valid for a closed volume of water which is in thermal equilibrium with vapor, therefore, the actual pressure will be lower.

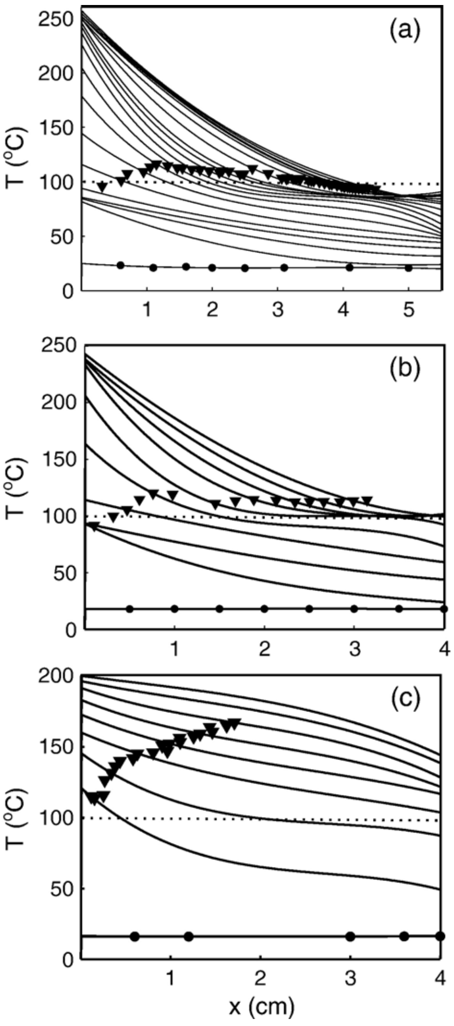

Fig. 5. Measured temperature profiles for (a) fired-clay brick, (b) calcium-silicate brick and (c) concrete. The vertical axis corresponds to the temperature, and the horizontal axis is the position in the sample. Initially the temperature of the sample is 20 °C. The surface is heated and the temperature increases in the whole sample. The temperature at the drying front as a function of the position of the drying front is also shown (▼). The horizontal dashed line indicates 100 °C. The positions of the thermocouples are indicated with dots (●).

5.3. Comparison with the model

For each sample the position of the drying front is determined as the point of maximum slope in moisture distribution, shown in Figs. 6a, b and c (●). As a reference, the position of the 100 °C isotherm is included as well (dashed line). Using the measured temperature distributions, instead of Eq. (1) combined with Eq. (5), we have calculated the predicted position of the drying front. The unknown permeabilities of the samples have been used as a fitting parameter, with a fixed porosity. For the saturation S_0 in the wet part the measured saturation to the right of the drying front is used. Excellent agreement with experiment has thus been obtained for concrete and calcium-silicate brick, with permeabilities well within the expected (literature) values. For concrete with a porosity of 7% a permeability of 5.10^{-17} m^2 was found to give optimal results, for calcium-silicate brick (porosity 20%) a

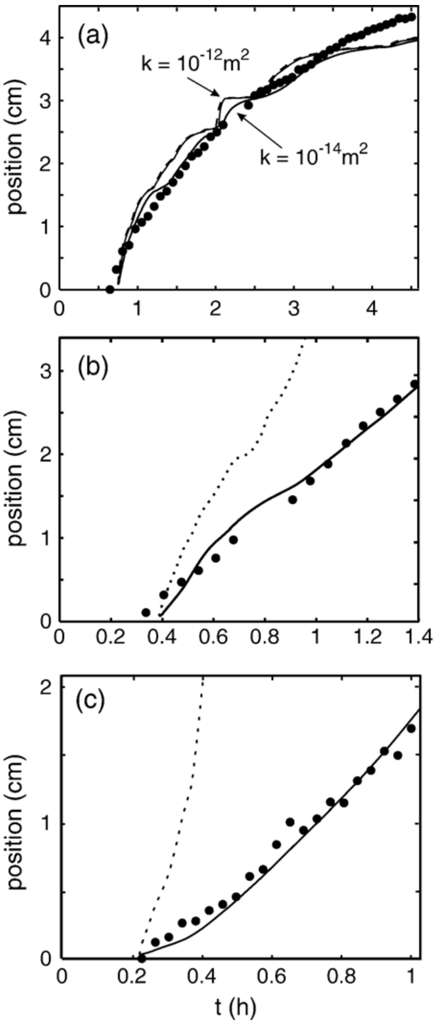

Fig. 6. Measured position of the drying front, indicated with ● for (a) fired-clay brick, (b) calcium-silicate brick and (c) concrete. As a reference the position of the 100 °C front is shown with a dashed curve. The position of the drying front resulting from the model calculations is shown by a solid curve. For fired-clay brick two model results are shown to illustrate the small difference between a permeability of 10^{-12} and 10^{-14} m^2. The calculated positions from the model correlate very good with the measured positions.

permeability of 5.10^{-15} m^2 and for fired-clay brick (porosity 25%) a permeability of 10^{-14} m^2. For fired-clay brick the permeability resulting from the model prediction differs by a factor of 100. However, the difference between the drying front predictions and the 100 °C isotherm diminishes for relative high permeabilities. The difference in drying front movement resulting from the model for permeabilities of 10^{-12} m^2 and 10^{-14} m^2 is small (see Fig. 6a). This means that the movement of the drying front in materials such as fired-clay brick is not limited by the transport of vapor from the drying front to the surface, as should be expected.

6. Conclusions and further research

It is possible to measure non-destructively the moisture distributions with NMR inside building materials during intense heating. The results of the present measurements already show that very interesting information can be obtained from the moisture and temperature profiles. They indicate that pressures close to the tensile strength of concrete can be generated by vaporization processes alone. Therefore, we conclude that moisture is one of the key parameters for understanding fire-spalling. The heating rate, permeability and pore size distributions determine the position of the drying front with respect to the 100 °C front. If the drying front lags behind the 100 °C front the water is superheated, which results in an increased pressure.

The theoretical model accurately describes the movement of the drying front observed in the experiments. It has to be remarked that at high permeabilities, such as in fired-clay brick, the movement of the drying front is not limited by vapor transport to the surface and therefore relatively insensitive for the actual value of the permeability. Although several simplifying assumptions have been made, this model still contains a mechanism that causes high pore pressures. Deeper in the material, the water vapor generated at the drying front cannot leave the material fast enough and thus slows the movement of the drying front. However, the temperature in the material keeps on rising, and the liquid water in the pores becomes superheated, resulting in high pore pressures. The permeability, porosity and saturation of the material prove to be critical parameters in this model. For the high permeabilities typical of fired-clay brick, the drying front can move relatively unhindered through the material and pore pressures remain close to atmospheric. In more impermeable materials such as concrete the drying front is clearly lagged, indicative of superheated water and high pore pressures.

In future work, the model can be extended by taking moisture transport and vapor fluxes in the wet part of the material into account, providing a more accurate description of a construction situation. Currently the experimental setup is being extended with a larger birdcage coil, for measuring samples up to 80 mm in length. A longer sample will give a more realistic representation of situations in practice, and will further enhance the one dimensionality of the experiment. In the future the pressure will be measured simultaneously with the temperature and moisture profiles. The influence of w/c ratios and hence permeability/porosity on the drying behavior of cement pastes. The spalling behavior of different types of concrete, e.g., OC or HPC [21], and the influence of PP-fibres [22–24] are some examples that could be studied using the new NMR setup.

Acknowledgments

The authors wish to thank Jaap Feijen and Jef Noijen for the construction of the NMR setup. We also thank Frank van Oost for his contribution to the model. Part of this research was supported by the Dutch Technology Foundation (STW) and the TNO Built Environment and Geosciences.

References

[1] P.C. Aitcin, Cements of yesterday and today—concrete of tomorrow, Cement and Concrete Research 30 (9) (2000) 1349–1359.

[2] P. Kalifa, F.D. Menneteau, D. Quenard, Spalling and pore pressure in HPC at high temperatures, Cement and Concrete Research 30 (12) (2000) 1915–1927.

[3] P.C. Aitcin, The durability characteristics of high performance concrete: a review, Cement and Concrete Composites 25 (4–5) (2003) 409–420.

[4] G.A. Khoury, Effect of fire on concrete and concrete structures, Progress in Structural Engineering and Materials 2 (2000) 429–447.

[5] A.N. Noumowe, P. Clastres, G. Debicki, J.L. Costaz, Transient heating effect on high strength concrete, Nuclear Engineering and Design 166 (1) (1996) 99–108.

[6] J.H. Chung, R. Consolazio, Numerical modeling of transport phenomena in reinforced concrete exposed to elevated temperatures, Cement and Concrete Research 35 (3) (2005) 597–608.

[7] J. Benard, R. Eymard, X. Nicolas, C. Chavant, Boiling in porous media: model and simulations, Transport in Porous Media 60 (1) (2005) 1–31.

[8] D. Gawin, C.E. Majorana, B.A. Schrefler, Numerical analysis of hygro-thermal behaviour and damage of concrete at high temperature, Mechanics of Cohesive-Frictional Materials 4 (1) (1999) 37–74.

[9] K. Kopinga, L. Pel, One-dimensional scanning of moisture in porous materials with NMR, Review of Scientific Instruments 65 (12) (1994) 3673–3681.

[10] R.M.E. Valckenborg, L. Pel, K. Hazrati, K. Kopinga, J. Marchand, Pore water distribution in mortar during drying as determined by NMR, Materials and Structures 34 (2001) 599–604.

[11] H.S. Carslaw, J.C. Yaeger, Conduction of Heat in Solids, Clarendon Press, Oxford, 1959.

[12] Y. Anderberg, Nist Special Publication 919: Spalling Phenomena of HPC and OC, 1997, pp. 69–73.

[13] Y. Ichikawa, G.L. England, Prediction of moisture migration and pore pressure build-up in concrete at high temperatures, Nuclear Engineering and Design 228 (1–3) (2004) 245–259.

[14] W. Kast, C.R. Hohenthanner, Mass transfer within the gas-phase of porous media, International Journal of Heat and Mass Transfer 43 (2000) 807–823.

[15] R. Perry, D. Green, Perry's Chemical Engineers' Handbook, McGraw-Hill, 1999.

[16] F.A. Ali, A. D.O'Connor, Explosive spalling of high-strength concrete columns in fire, Magazine of Concrete Research 53 (3) (2001) 197–204.

[17] E.L. Hahn, Spin echoes, Physical Review 80 (4) (1950) 580–602.

[18] M.T. Vlaardingerbroek, J.A. den Boer, Magnetic Resonance Imaging, 3rd editionSpringer Verlag, 2003.

[19] K.R. Brownstein, C.E. Tarr, Importance of classical diffusion in NMR studies of water in biological cells, Physical Review A 19 (6) (1979) 2446.

[20] C. Hall, W.D. Hoff, Water Transport in Brick, Stone, and Concrete, 1st editionSpon Press, London, 2002.

[21] F. Ali, Is high strength concrete more susceptible to explosive spalling than normal strength concrete in fire? Fire and Materials 26 (3) (2002) 127–130.

[22] A. Noumowe, Mechanical properties and microstructure of high strength concrete containing polypropylene fibres exposed to temperatures up to 200 °C, Cement and Concrete Research 35 (11) (2005) 2192–2198.

[23] P. Kalifa, G. Chene, C. Galle, High-temperature behaviour of HPC with polypropylene fibres—from spalling to microstructure, Cement and Concrete Research 31 (10) (2001) 1487–1499.

[24] C.G. Han, Y.S. Hwang, S.H. Yang, N. Gowripalan, Performance of spalling resistance of high performance concrete with polypropylene fiber contents and lateral confinement, Cement and Concrete Research 35 (9) (2005) 1747–1753.